2017

TORQUE RESPONSE OF THIN-FILM FERROMAGNETIC PRISMS IN UNIFORM MAGNETIC FIELDS AT MACRO AND MICRO SCALES

Soroosh Torabi

University of Kentucky, s.torabi@uky.edu

Digital Object Identifier: https://doi.org/10.13023/ETD.2017.345

TORQUE RESPONSE OF THIN-FILM FERROMAGNETIC PRISMS
IN UNIFORM MAGNETIC FIELDS AT MACRO AND MICRO SCALES

THESIS

A thesis submitted in partial fulfillment of the
Requirements for the degree of Master of Science in
Mechanical Engineering in the College of Engineering
At the University of Kentucky

By

Soroosh Torabi

Lexington, Kentucky

Director: Dr. Christine Ann Trinkle, Professor of Mechanical Engineering

ABSTRACT OF THESIS

TORQUE RESPONSE OF THIN-FILM FERROMAGNETIC PRISMS
IN UNIFORM MAGNETIC FIELDS AT MACRO AND MICRO SCALES

The non-contact nature of magnetic actuation makes it useful in a variety of microscale applications, from microfluidics and lab-on-a-chip devices to classical MEMS or even microrobotics. Ferromagnetic materials like nickel are particularly attractive, because they can be easily deposited and patterned using traditional lithography-based microscale fabrication methods. However, the response of ferromagnetic materials in a magnetic field can be difficult to predict. When placed in a magnetic field, high magnetization is induced in these ferromagnetic materials, which in turn generates force and/or torque on the ferromagnetic bodies. The magnitude and direction of these forces are highly dependent on the type of material used, the volume and aspect ratio of the ferromagnetic material, as well as the spatial distribution and magnitude of the magnetic field. It is important to understand these complex interactions in order to optimize force and torque generated, particularly given common limitations found in microfabrication, where it is often challenging to deposit large volumes of ferromagnetic material using conventional microdeposition methods, and power availability is also often limited, which in turn limits the ability to generate strong electromagnetic fields for actuation.

This work represents a theoretical analysis and experimental validation in macro scale to determine best practices when designing ferromagnetic actuators for microscale applications. Specifically, the use of nickel thin film prisms actuated in spatially uniform electromagnetic fields. These constraints were chosen because uniform magnetic fields can be readily generated with a simple and inexpensive Helmholtz coil design, and the uniformity makes actuation force independent of location, minimizing the need for spatial precision in devices. Nickel can also be easily deposited using evaporation or sputtering, generally in forms of thin-films.

KEYWORDS: Magnetic Torque, Ferromagnetic Thin-Films, Macro/Micro Actuation, Microrobotics

Soroosh Torabi
Author's Signature

July 18, 2016
Date

TORQUE RESPONSE OF THIN-FILM FERROMAGNETIC PRISMS

IN UNIFORM MAGNETIC FIELDS AT MACRO AND MICRO SCALES

By

Soroosh Torabi

Christine Ann Trinkle
Director of Thesis

Dr. Haluk Karaca
Director if Graduate
Studies

July 18, 2016
Date

ACKNOWLEDGMENTS

TABLE OF CONTENTS

LIST OF TABLES

TABLE OF FIGURES

Chapter 1 Introduction

1.1 Motivation

The non-contact nature of magnetic actuation makes it useful in a variety of microscale applications, from microfluidics and lab-on-a-chip devices to classical MEMS or even microrobotics. Ferromagnetic materials like nickel are particularly attractive, because they can be easily deposited and patterned using traditional lithography-based microscale fabrication methods. However, the response of ferromagnetic materials in a magnetic field can be difficult to predict. When placed in a magnetic field, high magnetization is induced in these ferromagnetic materials, which in turn generates force and/or torque on the ferromagnetic bodies. The magnitude and direction of these forces are highly dependent on the type of material used, the volume and aspect ratio of the ferromagnetic material, as well as the spatial distribution and magnitude of the magnetic field. It is important to understand these complex interactions in order to optimize force and torque generated, particularly given common limitations found in microfabrication, where it is often challenging to deposit large volumes of ferromagnetic material using conventional microdeposition methods, and power availability is also often limited, which in turn limits the ability to generate strong electromagnetic fields for actuation.

This work represents a theoretical analysis and experimental validation in macro scale to determine best practices when designing ferromagnetic actuators for microscale applications. Specifically, the use of nickel thin film prisms actuated in spatially uniform electromagnetic fields. These constraints were chosen because uniform magnetic fields can be readily generated with a simple and inexpensive Helmholtz coil design, and the uniformity makes actuation force independent of location, minimizing the need for spatial precision in devices. Nickel can also be easily deposited using evaporation or sputtering, generally in forms of thin-films.

In the theoretical analysis, a uniform magnetization approximation was used to derive induced magnetic torque on low aspect ratio ferromagnetic prisms. This was used to analytically determine the optimum ferromagnetic thin-film aspect ratio (R) and orientation (θ) to maximize induced magnetic torque. In order to experimentally validate these findings, cantilever beams with nickel tip masses were fabricated using wire EDM and placed in a uniform electromagnetic field so that the beam deflection could be used to indirectly measure the induced torque on the nickel. In both the analytical and experimental models, the maximum torque and maximum beam deflection was achieved at an aspect ratio of around 1:3 (thickness:width), but there was still a significant torque achieved even at much lower aspect ratio values. This is significant because for most microfabrication methods it is difficult and time consuming to make thick ferromagnetic structures. The results of these analyses can be used for rational, optimized design of microscale ferromagnetic actuators.

To further investigate the validity of the formulation for induced torque on thin-film ferromagnetic materials in micro scale, microscale cantilever beams were fabricated and tested in a uniform magnetic field. The microscale beams were made of a lithographically-patterned photopolymer with a thin-film of nickel deposited at the tip using sputtering and electroless nickel plating (ENP). When placed in a uniform magnetic field, the microscale beam deflection was observed by microscope as an indirect measurement of the induced torque on the thin film and was compared to the analytical results.

1.2 Thesis Organization

This thesis consists of five chapters with the following content:

Chapter one includes a brief introduction to the thesis by providing motivation and rational for the presented research.

Chapter two describes a conceptual and theoretical analysis of the physics of ferromagnetic materials response in a magnetic field. First, different materials are categorized based on their magnetic properties and their behavior in the magnetic fields are discussed. Then, more details on the advantages of using ferromagnetic materials in magnetic fields are presented. The induced magnetization in the ferromagnetic objects is explored both from a physical and mathematical stand point and the corresponding induced torque and force are discussed. Then, for a specific case of a ferromagnetic prism, the magnetization vector is calculated as a function of the object's aspect ratio. As a result, the maximum torque is achieved for the optimum values of the aspect ratio, object orientation angle in the magnetic field and the magnetic field strength.

Chapter three presents an experimental method to measure the induced torque on a ferromagnetic prism. Euler-Bernoulli beam theory is used to calculate the deflection of a paramagnetic macroscale cantilever beam with a ferromagnetic prism affixed to the tip in a spatially uniform magnetic field. Also, macro scale beams with different aspect ratio ferromagnetic prism were created to experimentally validate the predicted beam deflection values.

Chapter four involves the proof of concept for fabrication of ferromagnetic thin films for non-contact actuation. The fabrication process of microscale beams with thin film nickel fixed at the tip using electroless nickel plating (ENP) is described. Also, the beam deflection of the fabricated microscale beams is measured in a uniform magnetic field and is compared to the analytical prediction using the beam bending theory.

Chapter five provides a summary of the performed work and lays out future work for this project.

Chapter 2 Theory

2.1 Behavior of Materials in an Externally Applied Magnetic Field

All materials consist of atoms as their building blocks and each atom is made of a nucleus and a group of orbiting electrons. The electrodynamics dictates that the rotation of each negatively charged electron generates a magnetic dipole moment. Therefore, the network of atoms forms many micro domains within the material, with each having a random magnetic dipole moment. In most materials, the dipole moments of these micro domains neutralize each other and it results in no net magnetic field. On the other hand, in a permanent magnetic material, most of the micro domains' magnetic dipole moments are fixed in a certain direction, generating a magnetic field inside and around the object.

Materials can be categorized in three groups based on their magnetic properties: 1) diamagnetic, 2) paramagnetic and 3) ferromagnetic materials. In diamagnetic materials such as quartz and calcite, atoms do not have a net magnetic moment and therefore, there is a non-cooperative interaction between orbiting electrons when the body is placed in a magnetic field. In paramagnetic bodies, atoms have net magnetic moments that are partially and individually affected by an external magnetic field and they are reversed to their original alignment when the field is removed. In contrast with the first two groups, ferromagnetic materials have large micro domains with great parallel magnetic moments. These micro domains align spontaneously and to a great extent in the presence of an external field, and if the applied field is removed, the original orientation is restored. However, if the external magnetic field is great enough, the induced alignment remains even after the magnetic field is removed. The unique magnetic properties of ferromagnetic materials make it possible to generate force and/or torque on ferromagnetic

materials by applying an external magnetic field – a property that is useful in a variety of magnetic actuators and sensors.

If an object is placed in a magnetic field, $\vec{H}$, the dipole moments of the micro domains within the body tend to align with the external magnetic field. The induced alignment of the dipole moments creates a net magnetic moment in the material, $\vec{M}$. The induced magnetic moment (magnetization) is a vector quantity and is a measure of the object's tendency to align with the applied external field. When placed in a magnetic field, diamagnetic and paramagnetic materials exhibit zero or very low magnetization, whereas for ferromagnetic materials such as iron, cobalt and nickel, the induced magnetization can be very high. The interaction of $\vec{H}$ and $\vec{M}$ have the potential to generate forces and/or torques on the ferromagnetic object.

If the magnitude of the applied magnetic field is low enough, the magnetization vector for a ferromagnetic object will return to zero after the field is removed, as shown by the red curve in Figure 2.1. This corresponds to the magnetic micro domains within the material resuming random orientation with respect to on another. However, if the magnitude of the applied magnetic field exceeds a specific value, H_s, the magnetization vector of the object becomes saturated and pinned in the direction of the applied field. Increasing the external field beyond this point does not change the magnitude of the magnetization further; instead, it remains at the magnitude achieved at the saturation point, referred to as saturation magnetization, M_s. If the external field is removed, the magnetization cannot completely recover its original alignment and a residual magnetization, M_r, remains in the body, as shown in Figure 2.1. Note that neither the direction nor the magnitude of the residual magnetization vector are the same as the magnetization vector at saturation.

If the direction of the applied magnetic field is reversed on a ferromagnetic object with a residual magnetization, the material starts to demagnetize and lose the residual magnetization. If the reverse applied field is increased further, the ferromagnetic object saturates in the direction of the reversed field. Cyclic magnetization and demagnetization of the ferromagnetic material is referred to as the magnetic hysteresis and is shown by the green curve in Figure 2.1.
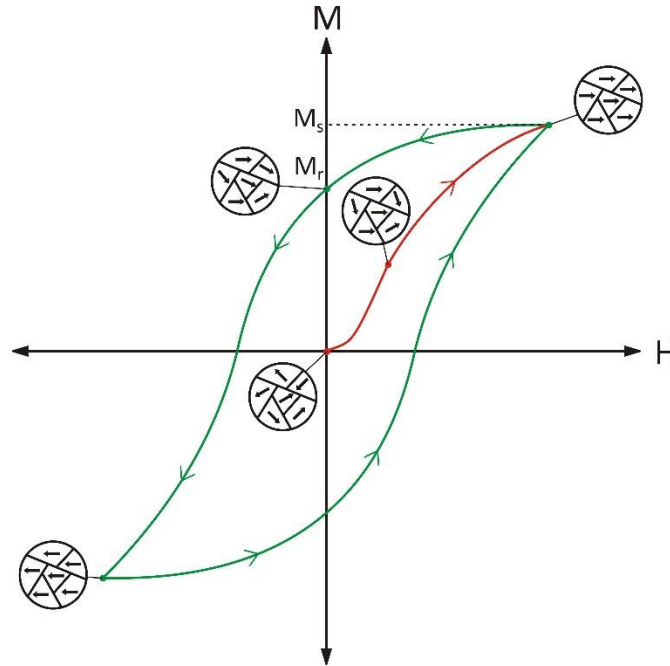
Figure 2.1 Induced magnetization in the ferromagnetic object vs the applied external field. Red curve shows the undersaturated region. Green curve shows the hysteresis loop of the ferromagnetic object.

When the ferromagnetic object is in the undersaturated region, the magnetization vector can be easily manipulated repeatedly by changing the magnitude of the applied field: removing the applied field causes the magnetization to return to zero. However, once a ferromagnetic object reaches saturation, the residual magnetization requires reversing the applied magnetic field to clear the "magnetic memory" of the object and return the magnetization to zero. Any nonzero residual magnetization within the object will cause the object to generate its own local magnetic field, which in turn can interfere with any new applied external magnetic field or the behavior of

other ferromagnetic objects within in the vicinity of the object. In applications that require control or actuation of multiple ferromagnetic objects, these residual fields can become very problematic. Therefore, the scope of this work will be focused on the undersaturation region where the magnetization of a ferromagnetic body can be reset by simply removing the applied field.

2.2 Ferromagnetic Materials in Undersaturated Magnetic Fields

When a ferromagnetic object is placed in a spatially non-uniform magnetic field, magnetic force is generated on the object. If the magnetized ferromagnetic object is considered as a magnetic dipole, the interaction of the magnetization vector with the gradient of the external field generates a force, $\vec{F}$, on the object:

$$\vec{F} = \mu_0 v(\vec{M}.\nabla)\vec{H} \tag{6.1}$$

Here μ_0 is the vacuum permeability ($\mu_0 = 4\pi \times 10^{-7} H/m$) and v is the ferromagnetic material volume.

The field generated by most magnets such as bar, horseshoe, or industrial electromagnets is highly nonuniform (Figure 2.2); the spatial gradients in these fields can be used to generate large amounts of force. It is also possible to generate spatially uniform fields, such as those associated with Helmholtz coil electromagnets (Figure 2.2) or the inside of a solenoid. Uniform magnetic fields are advantageous in many magnetic control and actuation applications, since the direction of the field can be easily manipulated and any forces or torques generated on the object are not location-dependent. However, equation (6.1) shows that if there is no spatial gradient in the applied magnetic field, the force generated on a ferromagnetic object placed within it is zero.
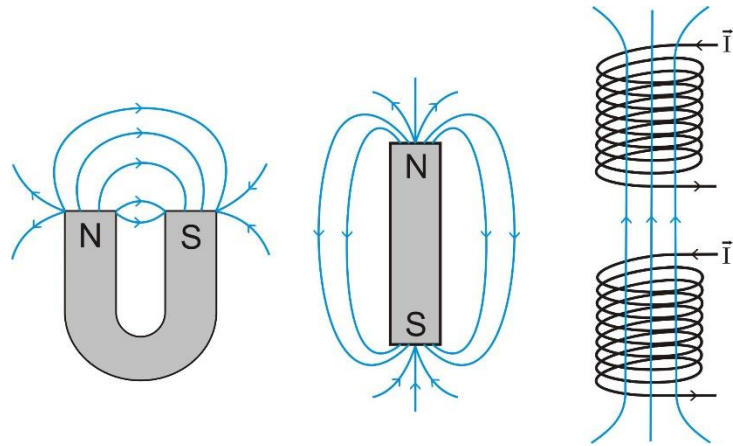
Figure 2.2 Schematic field lines in non-uniform magnetic fields (horseshoe and bar magnets) vs uniform magnetic fields (Helmholtz coil electromagnets).

On the other hand, magnetic torque, $\vec{T}$, is induced on a ferromagnetic object even in spatially-uniform magnetic fields. The magnetic torque is generated by the induced magnetization in the ferromagnetic body and is a function of the magnetization vector ($\vec{M}$) and the applied magnetic field vector ($\vec{H}$).

$$\vec{T} = \mu_0 v \vec{M} \times \vec{H} \tag{6.2}$$

Thus, in the presence of a known magnetic field, if the volume of the ferromagnetic object and the magnetization vector of the ferromagnetic body are known, it is possible to determine the value of the induced torque. Therefore, it is essential to know how to calculate the magnetization vector for a given object.

2.3 Determining the Magnetization Vector for a Ferromagnetic Object

The induced magnetic moment on a ferromagnetic object can be thought of a magnetic field inside the body, $\vec{H_\iota}$, which is in the same direction as the magnetization. The internal magnetic field and the magnetization vectors are related by the ferromagnetic material's susceptibility, X, which is a measure of the material's potential to be magnetized.

$$\vec{M} = X\vec{H_\iota}$$ (6.3)

Note that, below the saturation point, the internal magnetic field does not align perfectly with the external magnetic field. Therefore, it is assumed that a conceptual demagnetization field, $\overrightarrow{H_d}$, appears in the ferromagnetic body that prevents the internal field from completely matching the external field. Mathematically, this relationship can be shown as

$$\overrightarrow{H_\iota} = \vec{H} + \overrightarrow{H_d}$$ (6.4)

Figure 2.3 schematically illustrates the relation between these magnetic fields.
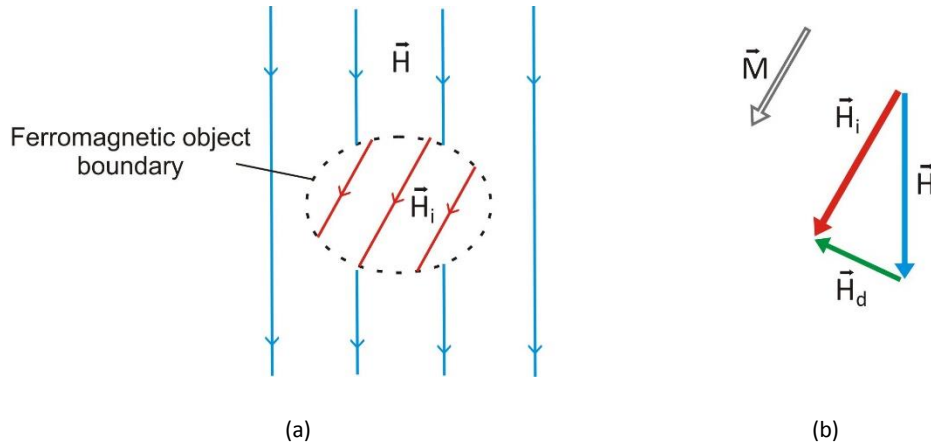
Figure 2.3 (a) schematic view of internal magnetic field, $\overrightarrow{H_\iota}$, vs applied external field, $\vec{H}$, (b) the vector relationship between the internal, external and demagnetization vectors.

If the demagnetization field is known, then the magnetization vector can be determined as a function of the external magnetic field, which is typically a known input parameter. To do so, a useful parameter is the symmetric demagnetization tensor, $\bar{\bar{N}}$, which represents the ratio of the strength of the material demagnetization field to the material magnetization.

$$\overrightarrow{H_d} = -\bar{\bar{N}}\vec{M}$$ (6.5)

By equating equations (6.3), (6.4), and (6.5), the magnetization can be written as

$$\vec{M} = X(\vec{H} - \bar{\bar{N}}\vec{M})$$ (6.6)

which can be solved for $\vec{M}$,

$$\vec{M} = \left(\frac{1}{X}\bar{\bar{I}} + \bar{\bar{N}}\right)^{-1} \vec{H} = \bar{\bar{X}}_a \vec{H} \tag{6.7}$$

Where $\bar{\bar{I}}$ is the identity tensor and $\bar{\bar{X}}_a$ is the apparent susceptibility tensor, which indicates the relationship between the external magnetic field and the magnetization within the ferromagnetic body. Equation (6.7) shows that the apparent susceptibility tensor not only determines the relative angle between the magnetic field and the magnetization vector, but it also affects the magnitude of the induced magnetization. Therefore, the apparent susceptibility tensor indirectly influences the cross product in equation (6.7) which determines the induced torque on the ferromagnetic body. Thus, it is important to understand how the apparent susceptibility tensor is computed, but for arbitrary geometries this can be prohibitively complicated.

The demagnetization tensor is symmetric by definition, and for a uniformly magnetized object the demagnetization tensor is constant throughout the body. In addition, Abbott, et al [1] showed that if the body coordinate frame is chosen to align with the principle axes of the ferromagnetic body, the resulting demagnetization tensor is always diagonal. So, for a uniformly magnetized ferromagnetic object with the Cartesian coordinate frame aligned with its main axes, the demagnetization tensor simplifies to

$$\bar{\bar{N}} = \begin{bmatrix} n_x & 0 & 0 \\ 0 & n_y & 0 \\ 0 & 0 & n_z \end{bmatrix} \tag{6.8}$$

where n_x, n_y and n_z are the demagnetization factors in the x, y and z directions, respectively. So, for a uniformly magnetized ferromagnetic object, the susceptibility tensor becomes:

$$\bar{\bar{X}}_a = \begin{bmatrix} \dfrac{X}{1+n_xX} & 0 & 0 \\ 0 & \dfrac{X}{1+n_yX} & 0 \\ 0 & 0 & \dfrac{X}{1+n_zX} \end{bmatrix} \qquad (6.9)$$

Among many different available shapes, ferromagnetic prisms (Figure 2.4a) are particularly interesting because they can be easily fabricated at both the macro and micro scales. And if the prism's susceptibility is low [2] and the dimensions are small relative to the applied magnetic field lines [3], the uniform magnetization assumption required for using equation (6.9) is valid for these geometries.

(a)   (b)
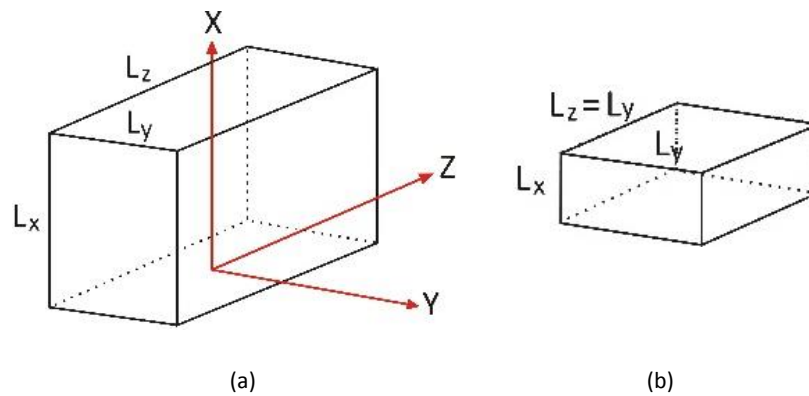
Figure 2.4 (a) prism vs (b) square cuboid.

Bellegia [4] was able to show that the demagnetization factors for a prism in a coordinate system aligned with major axes can be explicitly written as a function of the geometrical parameters of the body. For example, for the prism demagnetization factor in the z direction is

$$
\begin{aligned}
n_z = G(\lambda_x, \lambda_y) = \frac{1}{3\pi\lambda_x\lambda_y}\Big\{ &-2 + \lambda_y{}^3 + \lambda_x{}^3 + (2 - \lambda_y{}^2)\bar{\lambda}_y + (2 - \lambda_x{}^2)\bar{\lambda}_x \\
&- \bar{\lambda}_{xy}{}^3 + (-2 + \lambda_y{}^2 + \lambda_x{}^2)\Lambda - 3\lambda_y\, ln(\lambda_y + \bar{\lambda}_y) \\
&- 3\lambda_x\, ln(\lambda_x + \bar{\lambda}_x) + 6\lambda_x\lambda_y\, tan^{-1}\left(\frac{\lambda_x\lambda_y}{\Lambda}\right) \\
&- 3\lambda_x\lambda_y\, ln(\lambda_x{}^{\lambda_x}\lambda_y{}^{\lambda_y}) + 3\lambda_y(\lambda_x{}^2 - 1)\, ln\left(\frac{\bar{\lambda}_x}{\lambda_y + \Lambda}\right) \\
&+ 3\lambda_x(\lambda_y{}^2 - 1)\, ln(\frac{\bar{\lambda}_y}{\lambda_x + \Lambda}) + 3\lambda_y\lambda_x{}^2\, ln(\lambda_y + \bar{\lambda}_{xy}) \\
&+ 3\lambda_y{}^2\lambda_x\, ln(\lambda_x + \bar{\lambda}_{xy})\Big\}
\end{aligned}
\tag{6.10}
$$

where $\lambda_x \equiv L_x/L_z$ and $\lambda_y \equiv L_y/L_z$ with L_x, L_y and L_z are the lateral length of the prism in x, y

and z direction respectively. Also, $\bar{\lambda}_y \equiv \sqrt{1 + \lambda_y{}^2}$, $\bar{\lambda}_x \equiv \sqrt{1 + \lambda_x{}^2}$, $\bar{\lambda}_{xy} \equiv \sqrt{\lambda_x{}^2 + \lambda_y{}^2}$ and

$\Lambda \equiv \sqrt{1 + \lambda_x{}^2 + \lambda_y{}^2}$. Using the same methodology, n_y and n_x can be determined [4, 5], resulting

in

$$
n_z = G(\lambda_x, \lambda_y)
\tag{6.11}
$$

$$
n_y = G\left(\frac{\lambda_x}{\lambda_y}, \frac{1}{\lambda_y}\right)
\tag{6.12}
$$

$$
n_x = G\left(\frac{1}{\lambda_x}, \frac{\lambda_y}{\lambda_x}\right)
\tag{6.13}
$$

In addition, [6] showed that the trace of the demagnetization tensor is unity. As a result, the

demagnetization factors are constrained by

$$
n_x + n_y + n_z = 1
\tag{6.14}
$$

Therefore, any set of three of the previous four equations can be used to determine the three

demagnetization factors.

In the special case of a square cuboid, where at least two dimensions of the prism are equal (Figure 2.4b), these equations can be further simplified. For $L_y = L_z$, $\lambda_y = 1$, so

$$n_z = n_y = G(\lambda_x, 1) \tag{6.15}$$

And equation (6.14) can be rewritten as

$$n_x + 2n_y = 1 \tag{6.16}$$

If we further define the aspect ratio of the square cuboid as $R \equiv L_x/L_y \equiv L_x/L_z = \lambda_x$, then the demagnification factors can be stated as simple functions of this aspect ratio:

$$\begin{cases} n_x = G(R, 1) \\ n_y = n_z = 1 - 2n_x \end{cases} \tag{6.17}$$

Using these equations, n_x, n_y and n_z are shown as a function of the square cuboid aspect ratio in Figure 2.5. For a cube ($L_x = L_y = L_z$ and $R = 1$), the demagnetization factors are all equal to 1/3. However, if the aspect ratio of the square cuboid is smaller than 1, the demagnetization factor in the x direction increases whereas the demagnetization factors in the y and z directions both decrease. As the aspect ratio approaches zero—corresponding to a cuboid that is infinitely thin in the x direction—n_x approaches unity while the other factors go to zero.
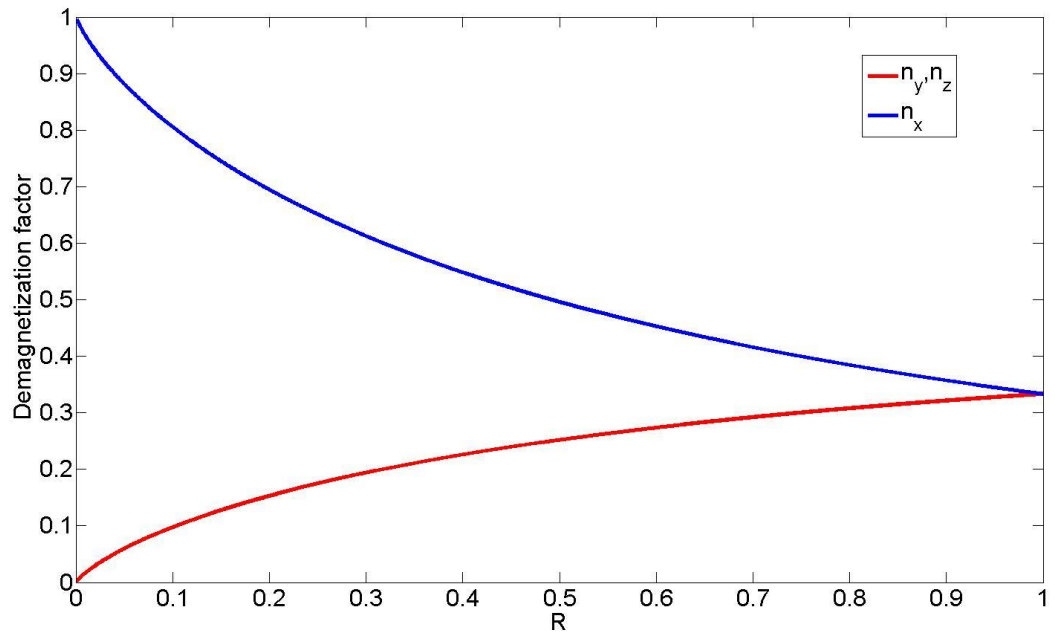
Figure 2.5 Demagnetization factors vs aspect ratio (R)

Once the demagnetization factors are known, the magnetization vector of a uniformly magnetized prism can be found:

$$\vec{M} = \left(\frac{X}{1 + n_x X} H_x, \frac{X}{1 + n_y X} H_y, \frac{X}{1 + n_z X} H_z\right) \tag{6.18}$$

where, H_x, H_y and H_z are the magnetic field components in x, y and z directions respectively. When the magnetization vector is known, equation (6.2) can be used to find the induced torque on a ferromagnetic body in a known magnetic field.

2.4 Magnetic Torque on a Ferromagnetic Prism in a Uniform Magnetic Field

Assume that the ferromagnetic square cuboid is oriented at an angle of θ with respect to a spatially uniform magnetic field, as shown in Figure 2.6.
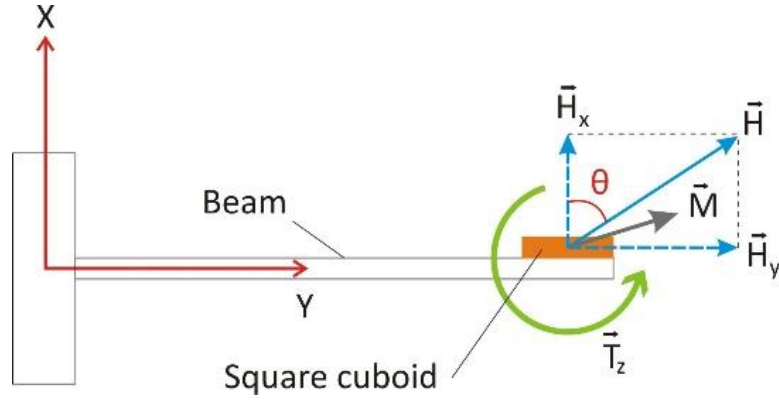
Figure 2.6 Orientation of a beam with a ferromagnetic square cuboid at the tip in a uniform magnetic field.

The magnetization induced in the prism interacts with the external field, which generates torque on the prism. Using equation (6.2), the torque about the z axis can be written as:

$$T_z = \mu_0 v(M_x H_y - M_y H_x) \tag{6.19}$$

Using equation (6.18), this can be rewritten as:

$$T_z = \mu_0 v H_x H_y X \left(\frac{1}{1 + n_x X} - \frac{1}{1 + n_y X} \right) \tag{6.20}$$

If the prism is oriented such that the external magnetic field component along the z axis is negligible

$(H_z = 0)$, this can be written as:

$$T_z = \frac{1}{2} \mu_0 v |\vec{H}|^2 X \left(\frac{1}{1 + n_x X} - \frac{1}{1 + n_y X} \right) sin2\theta \tag{6.21}$$

where $|\vec{H}|$ is the magnitude of the external magnetic field. Upon inspection of this equation, it can be seen that the magnitude of the applied torque is dependent on the geometry (v, n_x and

n_y, which are all functions of L_x, L_y and L_z) and the magnetic properties of the ferromagnetic material (X), as well as the magnitude ($|\vec{H}|$) and the orientation (θ) of the external magnetic field.

For a square cuboid with susceptibility of $X = 600$, with a lateral length of $30\ mm$ ($L_y = L_z = 30\ mm$) that is placed in a known external magnetic field such that the magnetic field component along the z axis is negligible, the torque about the z axis can be illustrated as a function of R as in Figure 2.7. For a cube ($L_x = L_y = L_z$ and $R = 1$), the induced torque is negligible. In this case, the demagnetization factors are equal in all principal directions and no net magnetization is generated in the body. However, the induced torque maximizes at the aspect ratio of 0.317. In other words, for a given footprint (L_y and L_z held constant) the maximum torque that can be generated on the prism occurs if the height of the cuboid is approximately one third of its lateral length.
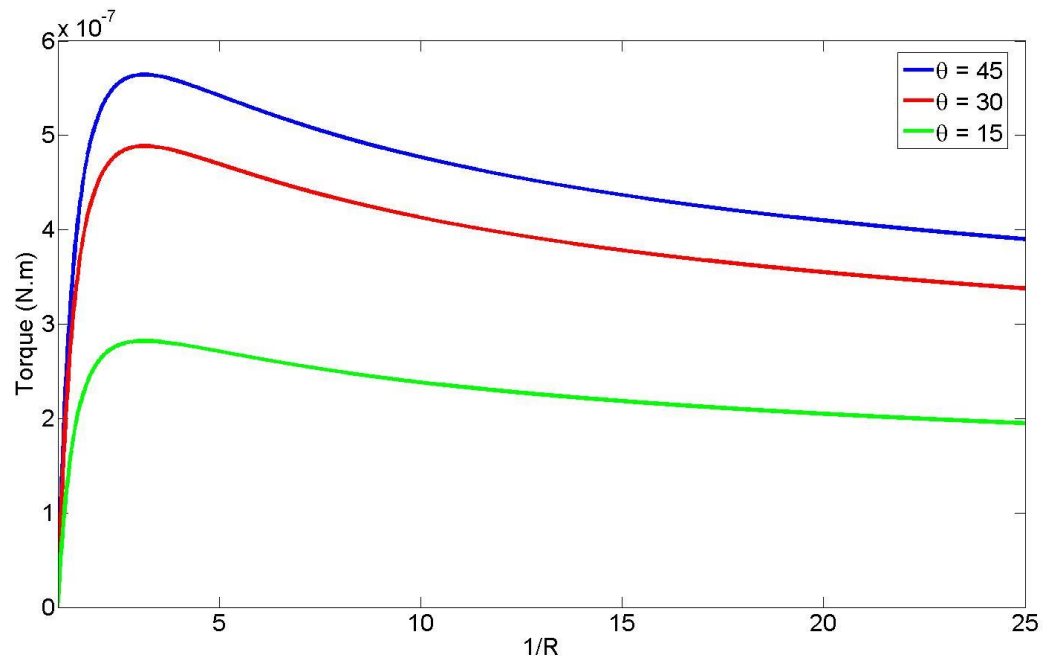
Figure 2.7 Torque vs aspect ratio (R) for different θs; for $l = 30mm$, $X = 600$, $|\vec{H}| = 4.2mT$.

Note that in the case of a square cuboid, higher aspect ratios correspond to a higher volume of the ferromagnetic material, which, in turn tends to generate more torque as shown in equation (6.21). On the other hand, the lower aspect ratios provide higher anisotropy in the ferromagnetic object, which leads to higher angles between the applied magnetic field and the magnetization vector. Therefore, the balance between the effective volume and the anisotropy of the object, at $R = 0.317$, maximizes the induced torque. Also, it is interesting to note that when aspect ratio is decreased below the optimum value, the induced torque initially decreases at a very slow rate. For example, if the thickness of the cuboid is reduced by 50% from the optimum thickness ($R: 0.317 \rightarrow 0.158$), the induced torque reduces only by 7.6%. This result is of a great significance at the microscale, where thin-film ferromagnetic square cuboids are relatively easy to fabricate compared to microfabrication of thicker ferromagnetic layers, which are often expensive, time consuming, and technically challenging to fabricate. Therefore, as shown in Figure 2.7, low aspect ratio thin films that are easier to fabricate can be used and still achieve relatively high induced torque.

In addition to being a function of geometry, magnetically induced torque is influenced by the field orientation (θ), as shown in Figure 2.8. Since the induced torque is a function of $sin2\theta$, it peaks at $\theta = 45°$. So if the principal axis of the square cuboid is at an angle of $45°$ with respect to the magnetic field direction, the maximum torque is achieved. At this angle, the x and y components of the magnetic field cooperate to maximize the interaction of the magnitude of the magnetization in the object and the relative angle between the magnetic field and the induced magnetization.

As shown in the same figure, torque is also proportional to the square of the external magnetic field magnitude ($|\vec{H}|$). From a physical stand point, higher magnetic field generates both a higher

magnetization and it also appears explicitly in the torque equation; the combination of the two effects results in a nonlinear behavior of the induced torque as the magnetic field increases.
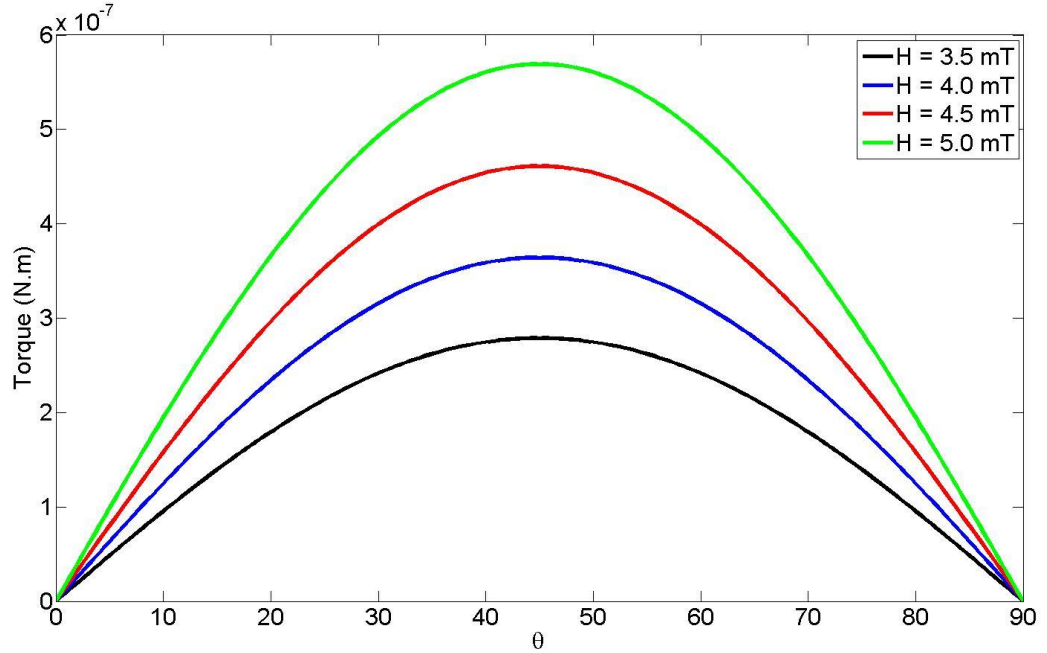
Figure 2.8 Torque vs θ for different magnetic fields; for $l = 30mm$, $X = 600$, $R = 0.11$.
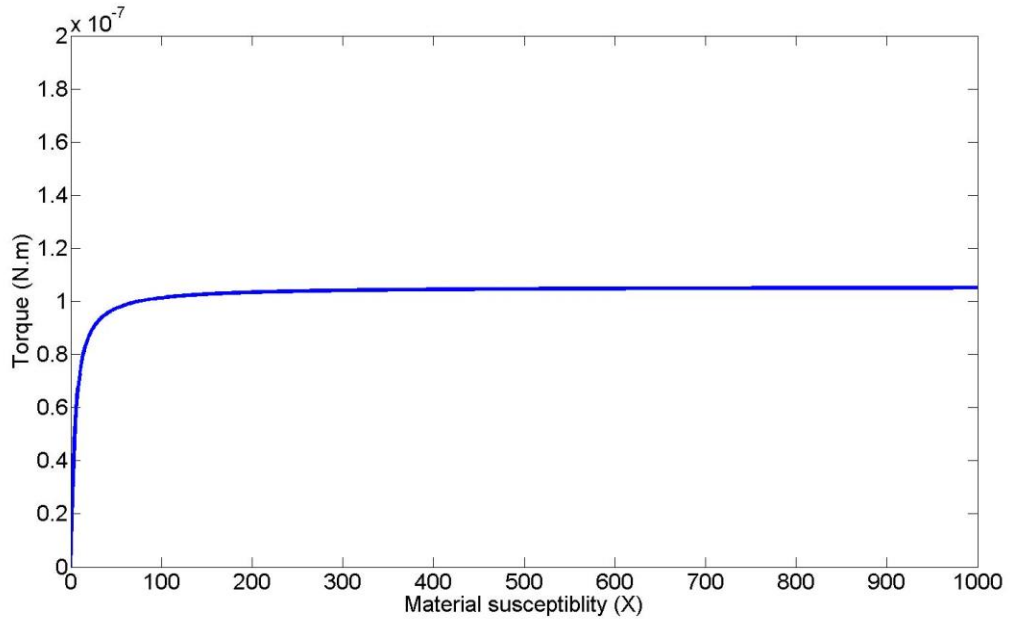
Figure 2.9 Torque vs material susceptibility (X); for $l = 30mm$, $\left|\vec{H}\right| = 4.2mT$, $R = 0.11$, $\theta = 45°$.

Torque can be plotted as a function of material susceptibility, as shown in Figure 2.9. It can be seen that for low susceptibility materials $X < 100$, the induced torque is strongly dependent on the material susceptibility; whereas for higher susceptibilities (i.e. $X \to \infty$), the diagonal elements of the apparent susceptibility tensors are close to a constant value for each direction. This results in the independent behavior of the induced torque for high susceptibility values, as shown in equation (6.22).

$$\bar{\bar{X}}_a(X \to \infty) \cong \begin{bmatrix} \dfrac{1}{n_x} & 0 & 0 \\ 0 & \dfrac{1}{n_y} & 0 \\ 0 & 0 & \dfrac{1}{n_z} \end{bmatrix} \tag{6.22}$$

Chapter 3 Macro-scale Beam Bending

As discussed in the previous chapter, an applied external magnetic field generates torque on a ferromagnetic object. For a case of a square cuboid in a spatially uniform magnetic field, the applied torque was formulated as a function of the magnetic field strength ($|\vec{H}|$), the aspect ratio of the cuboid (R), the susceptibility of the ferromagnetic material (X), and the orientation (θ) of the external magnetic field. However, torque is difficult to measure directly and in order to experimentally validate the formulation of the torque, an intermediate parameter is required. One way to indirectly measure torque is to use the torque to cause a measurable secondary effect: in this case, by affixing the ferromagnetic prism to the end of a cantilever beam. In the presence of an external field, the magnetic torque causes measureable bending of the beam, which can then be used to calculate the torque experienced by the prism.

3.1 Beam Bending of a Magnetically Actuated Beam

Euler-Bernoulli beam theory suggests that for pure bending of a long beam where transverse shear effects are negligible, the moment, $M_0(y)$, at each point along the length of the beam can be calculated as

$$M_0(y) = EI\frac{d^2\omega}{dy^2}$$

(7.1)

Where E, I and ω are the Young's modulus, the moment of inertia and the displacement of the beam respectively. In the special case of a moment applied at the end of a cantilever, as shown in Figure 3.1, Equation (7.1) can be solved for the maximum displacement, δ, at the end of the beam

$$\delta = \frac{M_0 l^2}{2EI} = \frac{6M_0 l^2}{Ebh^3} \qquad (7.2)$$

Where l, b and h are the beam length, width and height respectively.
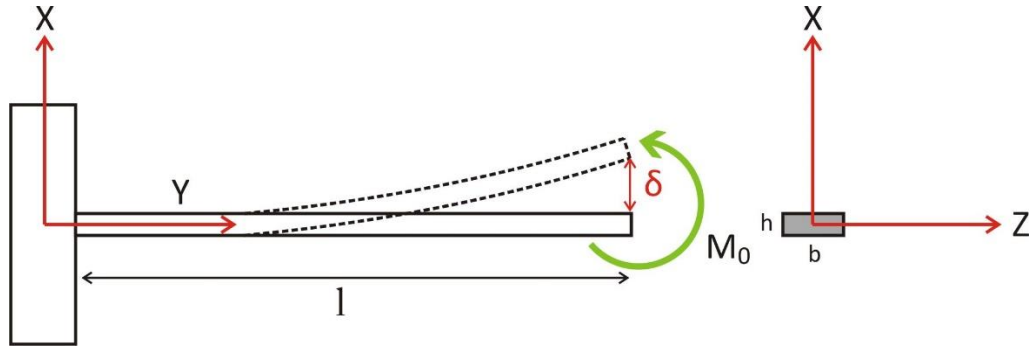
Figure 3.1 Beam bending of a cantilever.

If a ferromagnetic prism is attached to the tip of the cantilever and the whole system is placed in a uniform magnetic field, the magnetic torque that is induced in the ferromagnetic body will act as a moment on the cantilever and cause bending, as shown in Figure 3.1. If the applied moment is replaced with the induced magnetic torque on a ferromagnetic prism, the torque can be explicitly calculated as:

$$T_z = \frac{Ebh^3}{6l^2}\delta \qquad (7.3)$$

Therefore, if such a system is available and the end tip deflection is measured, this equation can be used to calculate the magnetic torque.

3.2 Fabrication & Experimental Setup

The experimental setup consisted of four different components: 1) a pair of electromagnetic Helmholtz coils used to generate a magnetic field, 2) a power source used to power the coils, 3)

cantilever beams with ferromagnetic prisms affixed to the free ends, and 4) a beam holder used to orient the beams within the magnetic field.

A pair of electromagnetic coils (Scientific Equipment and Services, Model EMU-75) were placed next to each other with a gap distance of $g = 55mm$. The distance between the two identical electromagnets was kept small compared to the core diameter ($d = 75mm$) in order to generate a uniform magnetic field between the magnets (Figure 3.2a). The magnetic coils were then connected to a (Hewlett Packard, Model E3631A) DC power source in order to generate the magnetic field with the control over the input voltage, V. The uniformity of the magnetic field was verified by measuring the magnetic field strength at different points between the coils using an axial probe Gaussmeter (Magnetic Instrumentation Inc, Model 912). The same Gaussmeter was used to measure the magnetic field strength generated at different voltages, the results of which are shown in Figure 3.2b.

The cantilever beams were cut using shears from thin aluminum alloy 1100 sheets (Lyon Industries, ASTM-B-209). Aluminum was selected because it is a paramagnetic material and is not affected magnetically when placed in a magnetic field. The ferromagnetic prisms were cut from a Ni-200 bar (McMaster-Carr) using wire EDM (Knuth, Smart EDM) in order to obtain nickel prisms with identical square cross sections but different thicknesses. The dimensions of the aluminum beams and the Ni prisms are shown in Table 3.1. Each Ni prism was glued to the tip of one of the aluminum beams. Figure 3.3 shows the nickel prisms after being cut (Figure 3.3a), the completed cantilever beams with nickel prisms attached (Figure 3.3b) and the wire EDM machine used to fabricate the prisms (Figure 3.3c).
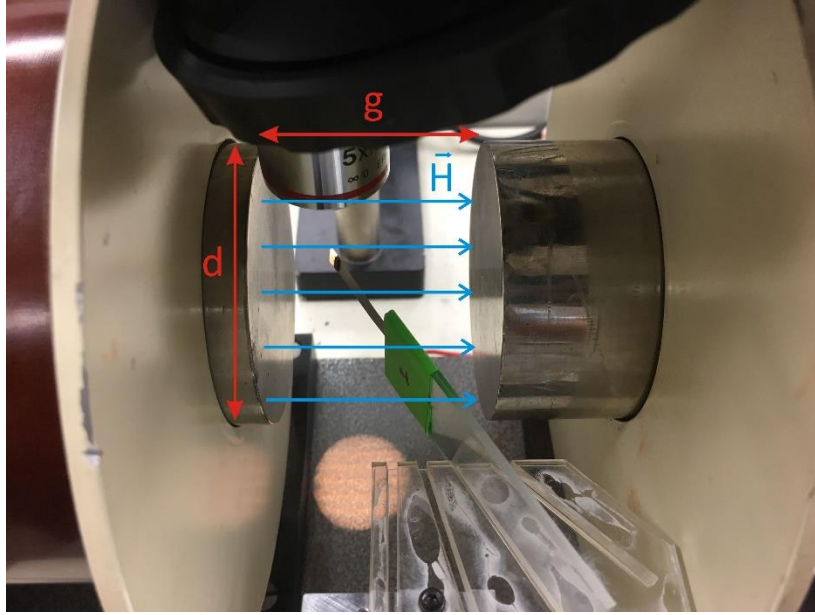
(a)
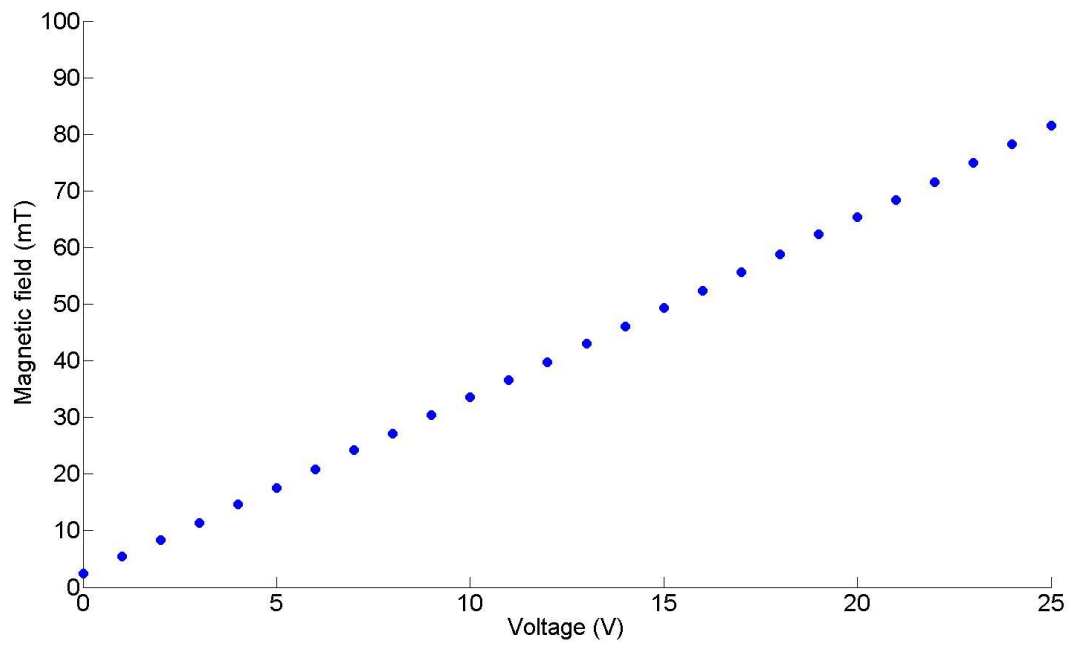
(b)

Figure 3.2 (a) coils diameter and gap, (b) Magnitude of the applied magnetic field $\left(\left|\vec{H}\right|\right)$ vs the input voltage (V) at a gap distance of $g = 55mm$.

Table 3.1 Dimensions of the Ni prisms glued to aluminum beams ($b = 5mm$, $h = 0.05mm$)

Sample #	Cantilever length (l)	Prism lateral length (L_y, L_z)	Prism thickness (L_x)	Prism aspect ratio (R)
1	$30mm$	$4mm$	$0.17mm$	0.04
2	$30mm$	$4mm$	$0.42mm$	0.11
3	$30mm$	$4mm$	$0.79mm$	0.20
4	$30mm$	$4mm$	$0.98mm$	0.25
5	$30mm$	$4mm$	$1.60mm$	0.40
6	$30mm$	$4mm$	$2.60mm$	0.65
7	$20mm$	$4mm$	$0.42mm$	0.11
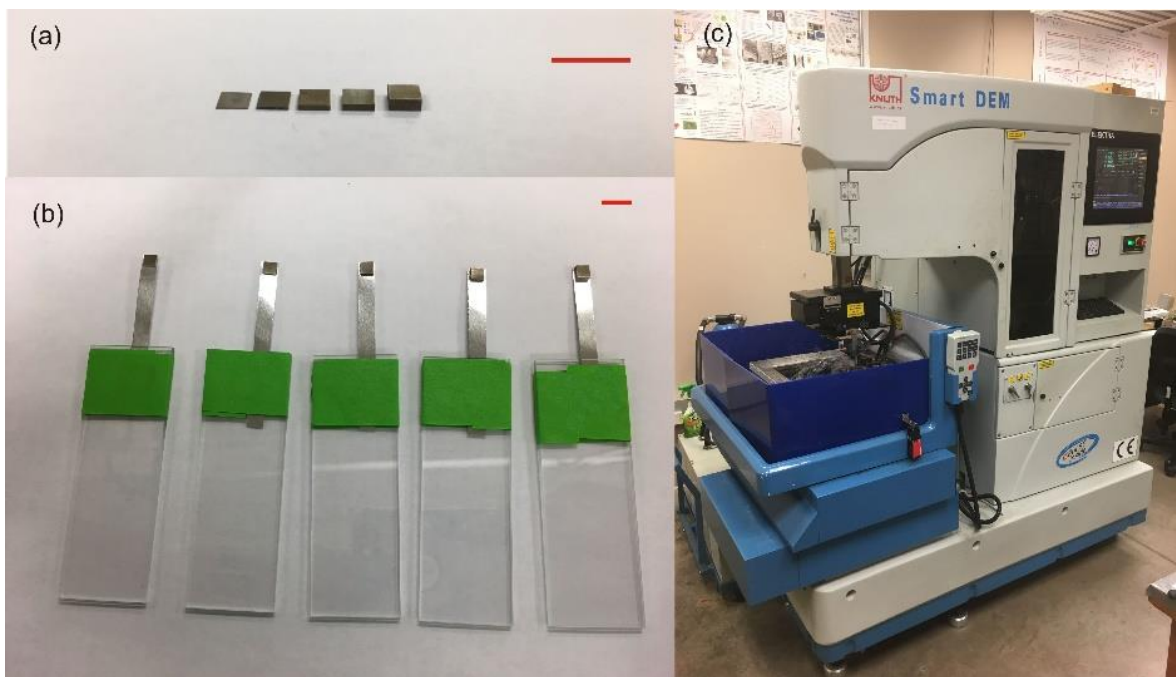
Figure 3.3 (a) Wire EDM cut Ni prisms, (b) clamped aluminum cantilevers with Ni prism at the tip between glass slides, (c) Wire EDM machine; scale bar = $10mm$.

The fixture shown in Figure 3.4 was used to position the beams within the magnetic field. The fixture allows the beams to be clamped between two glass slides, the orientation of which is controlled by a laser cut acrylic holder. All materials used in creating the fixture are paramagnetic, in order to minimize impact on the magnetic field, $\vec{H}$.
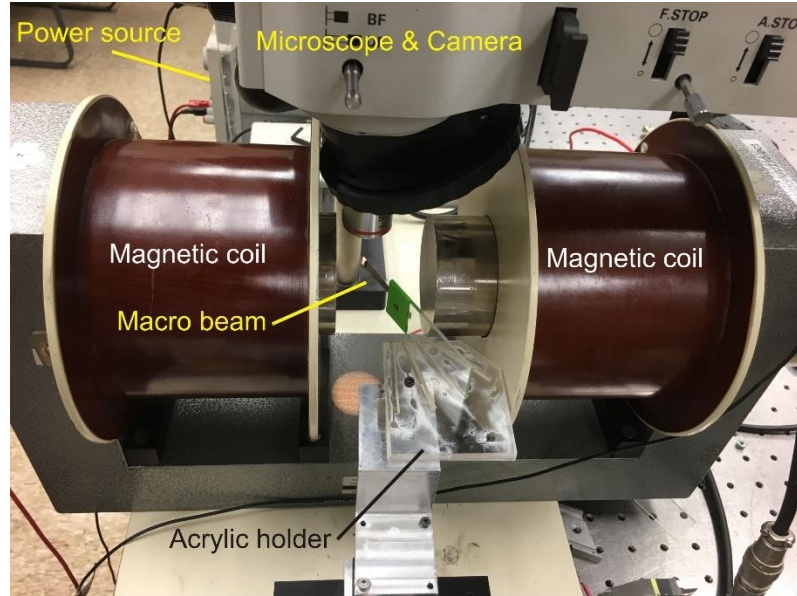
Figure 3.4 Experimental setup.

Each sample was placed in the magnetic field at three different angles ($\theta = 15°, 30°, 45°$) and four different magnetic fields ($|\vec{H}| = 0 \, mT, 8.4mT, 14.6mT, 20.8mT$). To measure the beam deflection at each trial, digital images of the beam were taken using a (Nikon, L-IM) microscope and (Olympus, QColor3) camera. ImageJ software was used to calculate the beam tip deflection with respect to the original beam orientation at $|\vec{H}| = 0 \, mT$, as shown in Figure 3.5.

(a)　　　　　　　　(b)　　　　　　　　(c)　　　　　　　　(d)
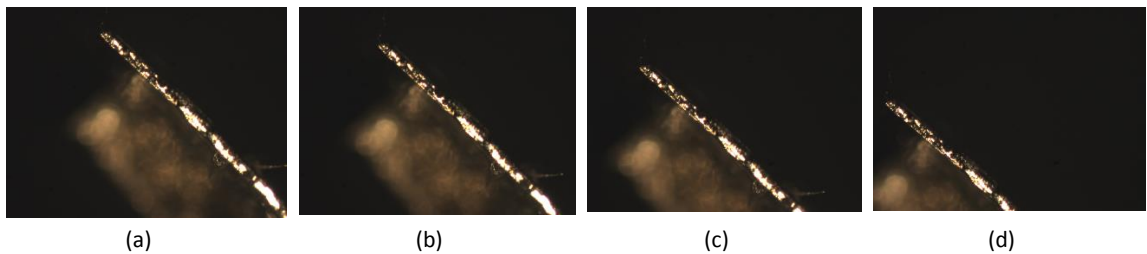
Figure 3.5 Digital images of the macro scale beam in the magnetic field at (a)$|\vec{H}| = 0mT$, (b) $|\vec{H}| = 8.4mT$, (c) $|\vec{H}| = 14mT$, (d) $|\vec{H}| = 20.8 \, mT$, for sample #7.

3.3 Results and Discussion

Figure 3.6 shows the beam deflection measurements as well as the theoretical predicted deflection as a function of the prism aspect ratio. Both the general trend and magnitude of the experimental measurements show generally good agreement with theory. The highest beam

deflection for the experimentally tested cantilevers was seen at a prism aspect ratio of 0.4, which

is similar to the analytically-predicted optimum value of 0.317. In the experimental results, the

beam deflection for low aspect ratio prisms was higher than the predicted values. In this range

for a lateral length of $4\,mm$, the lower aspect ratios correspond to relatively large prisms

compared to the magnetic field, which may violate the uniform magnetization assumption used

in deriving the magnetic torque relationships in Chapter 2.
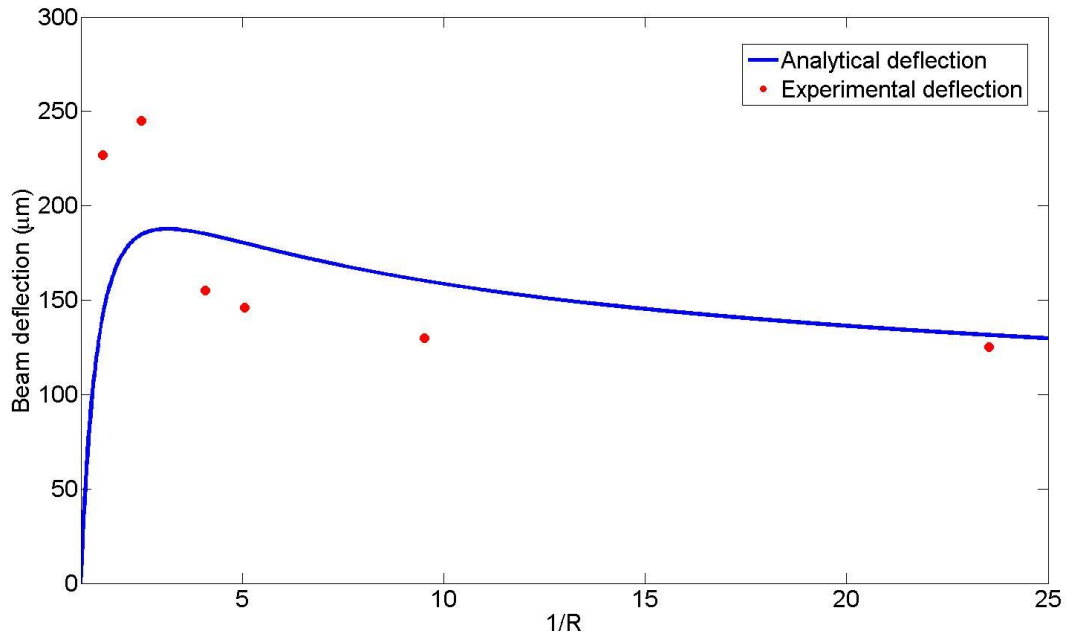
Figure 3.6 Experimental vs analytical beam deflections for different aspect ratios (R), $\left|\vec{H}\right| =$
$8.4mT \text{ and } \theta = 30°.$

Theoretical and experimental beam deflection for different magnetic field magnitudes is shown

Figure 3.7. These experimental results also show good agreement with the analytically predicted

behavior. The beam deflection is maximized when the principle axis of the beam (x axis) is aligned

at 45° with respect to the magnetic field lines, as predicted by theory. In addition, the

experimental beam deflections are higher when in the presence of higher magnitude magnetic

fields, which corresponds to the effect of the magnetic field in both the magnetization of the

ferromagnetic prisms and the induced torque. The measured experimental values are within an order of magnitude of theoretical predictions, but do not match exactly. The cantilever beam stiffness is highly sensitive to the Young's Modulus and dimensions of the beam; so even small fabrication errors in the beam or small inaccuracies in assumed material properties could result in a relatively large mismatch between the predicted and observed results.
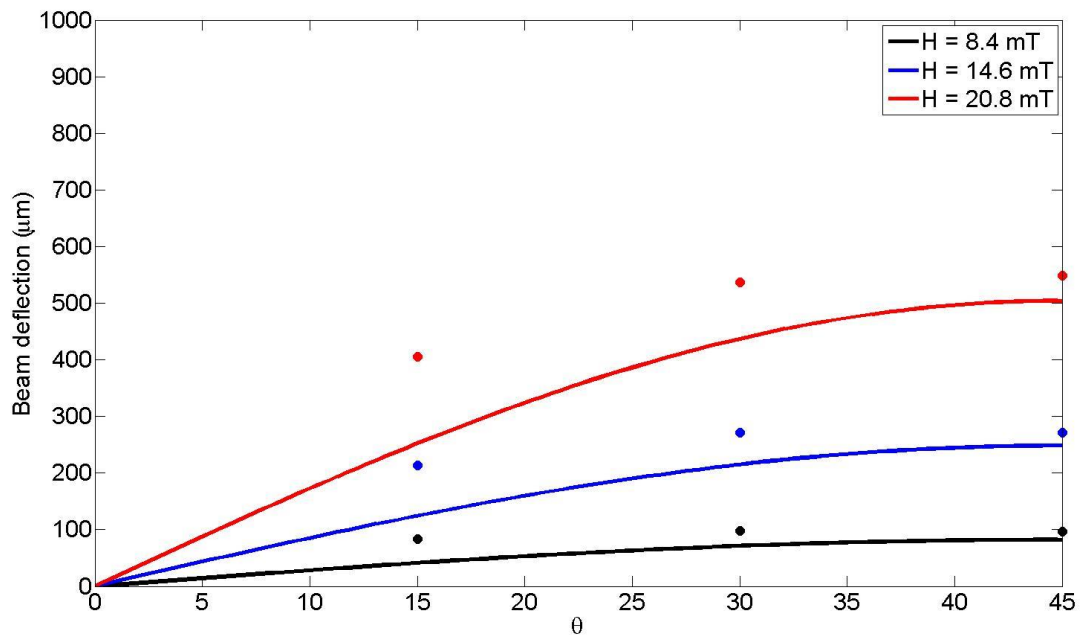
Figure 3.7 Experimental vs analytical beam deflections for different magnetic fields, sample #7

Chapter 4 Microbeam Fabrication and Bending

At the microscale, magnetic forces have been applied in a variety of applications for actuation and sensing. One embodiment uses microfabricated magnetic coils that use electric current to generate a magnetic field that interacts with either a permanent magnet or ferromagnetic object [7, 8]. However, these systems require both an onboard electrical circuit and a connected power supply, which typically limits the mobility of the system, making it impossible to create "untethered" or wire-free actuation. In addition, because the fabricated coils are often very small, these systems are only capable of generating very small, localized magnetic fields.

Another way to use magnetic force at the microscale involves remote actuation. In this case, a microscale magnetically responsive part is actuated in the presence of an externally applied magnetic field. With a strong enough field, the magnetically responsive material can be controlled and actuated from relatively large distances (tens of centimeters or more). This methodology has been used by a number of researchers to create remotely controlled dynamic systems in microrobotics [9-11]. For example, [12] created free standing beams with thin film nickel cobalt at the tip that could be remotely actuated to replicate the swimming motion of sperm. However, one of the main drawbacks of remote actuation is that when large force or torque generation is needed, these systems can require a relatively large volume of ferromagnetic material and/or very strong magnetic fields. The former is a particular problem, because most microfabrication methods are designed to create very thin (~ 1 μm) layers of material, so it can be technically challenging to generate thicker microscale ferromagnetic materials.

There are a variety of options for depositing ferromagnetic materials such as nickel at the microscale, including: thermal evaporation, chemical vapor deposition, sputtering, and electroplating. The first three methods are mostly used to fabricate thin film layers and deposition

of higher thickness of the material faces different challenges. Thermal evaporation and chemical vapor deposition can be used to deposit thin films of nickel; however, the high temperature and the chemical composition of the gasses used in these processes may not be compatible with other materials in the microfabricated part [13]. In addition, these processes, as well as sputtering, have very low deposition rates, which can make them time consuming and costly for fabrication of large volumes of ferromagnetic material. Higher deposition rates can be achieved by using electroplating, but this method requires a seed layer that must be electrically connected to a power supply during the deposition process. This makes it very difficult to create freestanding nickel "islands" on a surface, such as the nickel prisms required for this project.

Creating high-torque ferromagnetic microactuators required the development of a unique nickel microfabrication method. This method uses a combination of sputtering of a nickel seed layer onto photopolymer (SU-8) cantilever beams, combined with a modified electroless nickel plating method to deposit nickel in a confined prism geometry. Combining this with the equations derived in the previous chapters made it possible to create ferromagnetic prisms that were capable of generating very high torque—and therefore high beam deflection—without unreasonably long microfabrication times.

4.1 Beam Bending in Micro Scale

In this chapter, the same methodology presented for macro scale cantilevers is used to investigate the capability of the microscale nickel prisms to actuate a microscale cantilever beam in a spatially uniform magnetic field. The external magnetic field generates magnetization in the prism, which in turn generates a magnetic torque on the prism and the cantilever. Therefore, equation (4.1) can be used to predict the beam deflection in the presence of a magnetic field, which can in turn be used to calculate the induced magnetic torque.

$$\delta = \frac{6M_0L^2}{Ebh^3} = \frac{L^2}{Ebh^3} \cdot 3\mu_0 v \left|\vec{H}\right|^2 X \left(\frac{1}{1 + n_xX} - \frac{1}{1 + n_yX}\right) sin2\theta \qquad (8.1)$$

4.2 Fabrication

The fabrication process of a polymer cantilever with a nickel prism at the tip consists of three parts: 1) fabrication of the cantilever structure, 2) deposition of a nickel seed layer, and 3) depositing additional nickel using electroless nickel plating.

The polymer cantilever was created using photolithographic patterning of SU-8 photoresist. First, a sacrificial layer of Omni Coat was spin coated at 3000rpm for 30s on a silicon wafer (UniversityWafer) and the wafer was then baked at 250°C for 1min. Then, SU-8 3005 (MicroChem) was spin coated at 4000rpm for 30s on the wafer and the SU-8 was prebaked at 65°C and 95°C for 1min and 3mins respectively. A chrome photomask with the microbeam pattern was used to crosslink the prebaked SU-8 using UV light for 3mins at 2.8 mJ/cm^2. Then, the wafer was post-baked at 65°C and 95°C for 1min and 2mins respectively. Thereafter, the uncrosslinked SU-8 was removed using SU-8 developer (MicroChem) and the cantilever structure was defined. A schematic for the process and a micrograph of one of the resulting beams is shown in Figure 4.1.
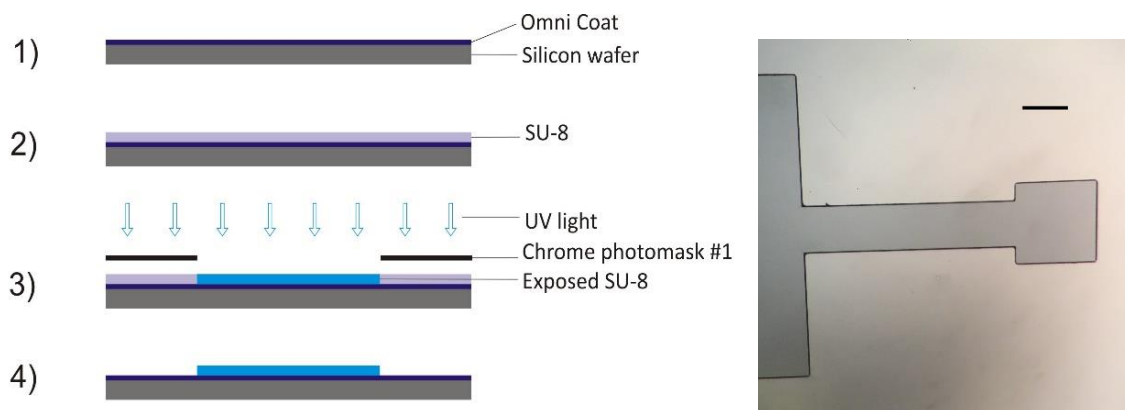

Figure 4.1 (Left) Fabrication process of the polymer microbeams, 1) deposition of the Omni Coat, 2) SU-8 deposition, 3) exposure of the SU-8 layer, 4) development of unexposed SU-8. (Right) Micrograph of fabricated SU-8 cantilever beam. Scale bar = 150μm.

Once the cantilevers were fabricated, the nickel prisms needed to be patterned at the end of the cantilevers. SU-8 is not compatible with high temperature processes such as thermal evaporation and chemical vapor deposition. The slow deposition rate for these processes and sputtering would have also required incredibly long deposition times. It also would have been incredibly difficult to create an electrical connection between the tip of the cantilever and a power source, so electroplating was not applicable. So, an alternative method was to use electroless nickel plating (ENP) where Ni is chemically reduced and deposited on a surface. The ENP process requires a seed layer such as Ni, Cr, Ti or Ta, and will not spontaneously deposit onto SU-8, making it promising for the patterning required here.

To pattern the seed layer on the SU-8 cantilever, positive photoresist S1813 (MicroChem) was used. S1813 was spin coated on the silicon wafer at 1000 rpm for 30 seconds, followed by a pre-exposure bake at 115℃ for 1min. Then, a second photomask was used to expose the positive photoresist for 1 min at 2.8 mJ/cm^2. The exposed positive photoresist was then removed by 1:1 diluted solution of water and the Microdeposit concentrate (MicroChem). After this development step, the SU-8 cantilever was masked with the positive photoresist with only the tip of the cantilever open for deposition of the seed layer.

The seed layer consisted of 50 nm thick tantalum adhesion layer followed by a 100 nm layer of nickel. These two layers were deposited using sputtering (Ta sputtering at $3.97 mTorr$, rate: $0.2 Å/s$; Ni sputtering at $4.37 mTorr$, rate $1.6 Å/s$). Following deposition, the positive photoresist masking layer was removed using acetone to prepare the cantilever with thin film Ni at the tip for the lift-off process using the ENP. A schematic for the seed layer sputtering steps of the process and a micrograph of one of the resulting beams is shown in Figure 4.2.
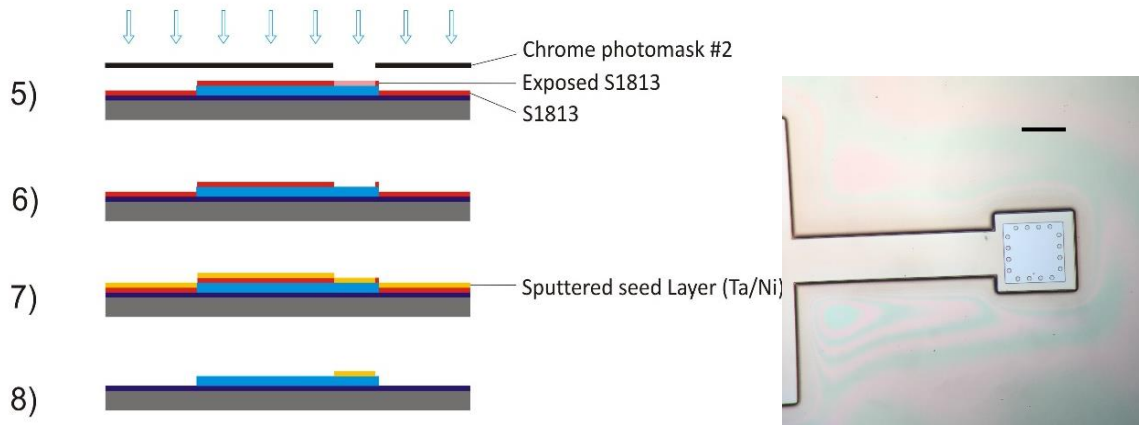
Figure 4.2 (Left) Fabrication process for creating nickel seed layer on the tips of the microscale cantilevers. 5) deposition and exposure of positive photoresist, 6) removal of the exposed positive photoresist, 7) sputtering the seed layer, 8) removal of the positive photoresist. (Right) Micrograph of SU-8 cantilever beam with sputtered nickel layer. Scale bar = $150\mu m$.

An ENP bath was prepared by heating 128 mL of purified DI water was heated to 91℃ on a hotplate. Then, 8 mL of part A and 24 mL of part B of a commercially available ENP kit (Casswell plating) were added to the bath. Once thermal equilibrium was achieved, the silicon wafer with the cantilever pattern was placed into the bath for 37 minutes. Then, the wafer was removed from the bath and was allowed to equilibrate to room temperature for 5 minutes, after which it was rinsed with DI water.

It was discovered that when this process was performed on cantilevers prepared as described, the sputtered seed layer almost always delaminated as shown in Figure 4.3; as a result, the final cantilevers had little to no nickel on the ends. One possible reason for the delamination is that the ENP process is thermally activated and the wafer was in the hot bath for extended time; the mismatch in the thermal expansion rates for SU-8 versus nickel may have caused stress to build between the layers eventually leading to delamination. In addition, the reduction reaction of nickel that occurs at the surface of the seed layer during ENP produces small bubbles of hydrogen. When these bubbles grow to sufficient size, buoyancy causes them to detach from the surface, which may exert additional force on the seed layer.
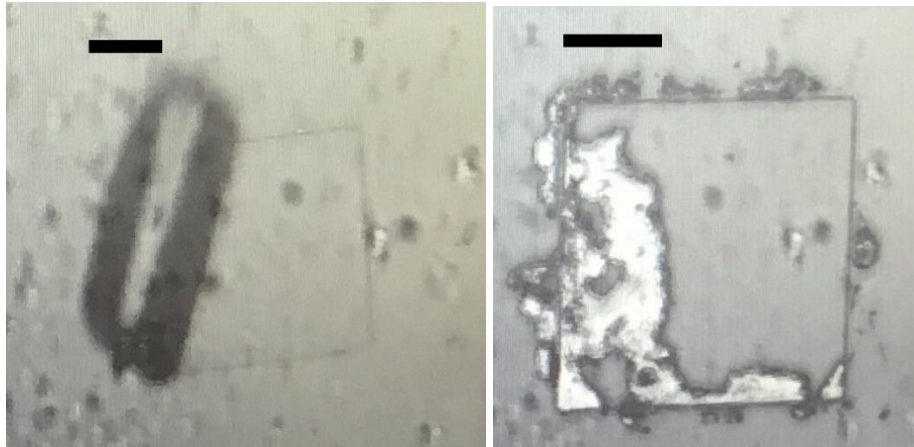
Figure 4.3 Delaminated seed layers during ENP process. Scale bar = $50\mu m$.

In order to prevent the delamination of the seed layer during the ENP process, a locking mechanism was developed. In this method, after the seed layer was sputtered on the cantilever and the positive photoresist was removed, using photolithography, a SU-8 frame was patterned on the edges of the seed layer so that it can physically hold the seed layer in place during the ENP process. Then, the ENP process was performed as mentioned above, and no delamination was observed. After fabrication, the cantilevers were released from the silicon substrate by chemically dissolving the Omni Coat base layer using Remover PG (MicroChem). These final stages of the fabrication process and a micrograph of a cantilever after the SU-8 frame patterning step are shown in Figure 4.4.
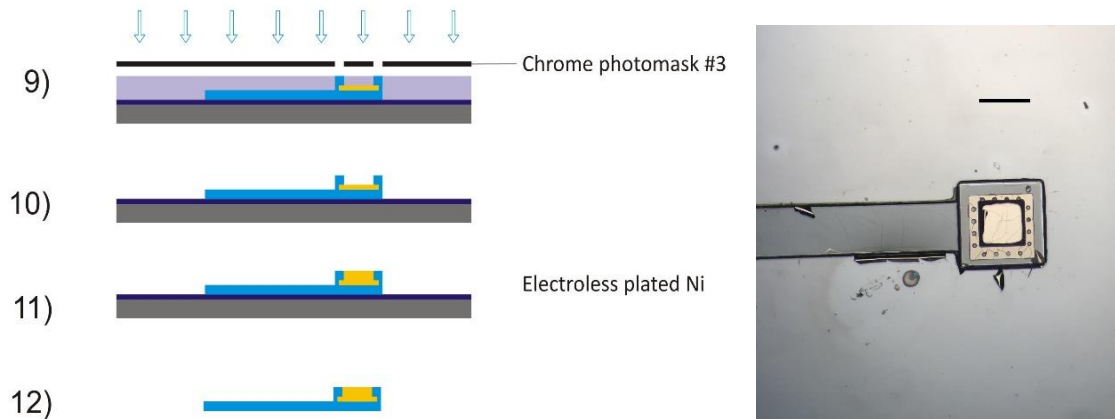
Figure 4.4 (Left) ENP process and cantilever release steps during microfabrication process: 9) deposition and exposure of the second SU-8 layer, 10) development of unexposed SU-8, 11) electroless Ni plating, 12) removal of the Omni Coat layer and release of the microbeam. (Right) Micrograph of SU-8 cantilever beam after step 10. Scale bar = $150\mu m$.

The thickness of the nickel deposited during the ENP process was measured using a Zygo interferometer, the results of which are shown in Figure 4.5. Table 4.1 shows the dimensions and the specifications of the SU-8 cantilever and the nickel prism, as measured using the Zygo and optical microscopy.

(a)   (b)
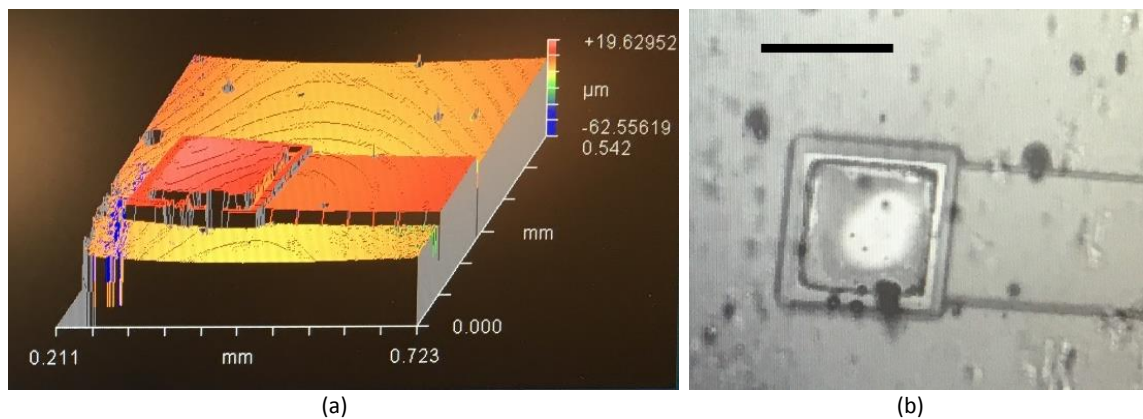
Figure 4.5 (a) Zygo measurement of the microbeams, (b) image of the electroless nickel plated microbeam. Scale bar = $150\mu m$.

Table 4.1 Microbeam geometry and material properties

Cantilever dimensions: length (l), thickness (h), width (b)	1 mm, 3.7 μm, 150 μm
Nickel thin film dimensions: L_x, L_y, L_z	30 μm, 150 μm, 150 μm
Aspect ratio (R)	0.2
Young's Modulus of SU-8 (E) [14]	4.4 GPaError! Bookmark not defined.

## 4.3 Experimental Setup and Results

The released cantilevers were then clamped and glued between glass slides so that they can be oriented at different angles in the magnetic field using the acrylic holder. The magnetic field was generated using the same experimental setup presented in the previous chapter. Each sample was placed in the magnetic field at three different angles ($\theta = 15°, 30°, 45°$) at three different magnetic fields ($\left|\vec{H}\right| = 30.4\ mT, 55.6\ mT, 81.6\ mT$). To measure the beam deflection at each trial, digital images of the beam were taken using a (Nikon, L-IM) microscope and (Olympus, QColor 3) camera. Then, ImageJ software was used to calculate the beam tip deflection with respect to the original beam orientation at $\left|\vec{H}\right| = 0\ m$, as shown in Figure 4.6.

(a)　　　　　　(b)　　　　　　(c)　　　　　　(d)
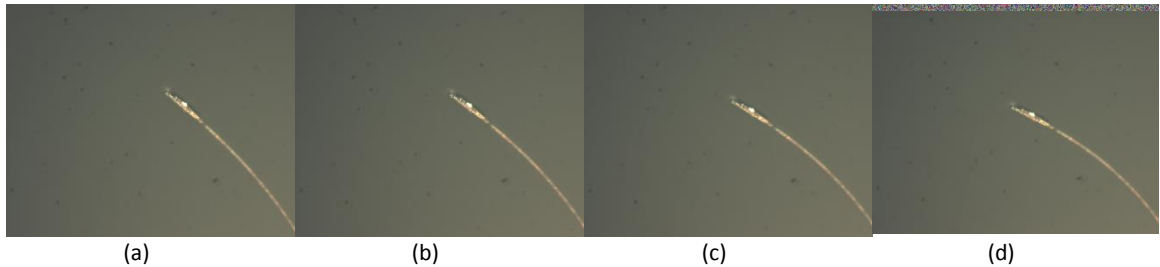
Figure 4.6 Digital images of the micro scale beam in the magnetic field at (a)$\left|\vec{H}\right| = 0mT$, (b) $\left|\vec{H}\right| = 30.4mT$, (c) $\left|\vec{H}\right| = 55.6mT$, (d) $\left|\vec{H}\right| = 81.6\ mT$.

Experimental beam deflection for different magnetic fields is shown Figure 4.7. It can be seen that the beam deflection at the microscale follows the same trend as the analytical solution: the deflection peaks at $\theta = 45°$ and increases with increased magnetic field strength. However, it is important to note that the magnitude of the deflection measured in the experiments is roughly

1/20th that predicted by the analytical solution. There are a number of reasons that could be causing the mismatch, including error in the material properties of the SU-8 and the electroless plated nickel and inaccuracies in measuring the cantilever and prism geometry. Also, since the ENP process involves nucleation of hydrogen bubbles, the deposited nickel may include cavities which reduce the effective volume of ferromagnetic material. Future work will focus on characterizing these errors and developing a more accurate predictive model for deflection of these microbeams.
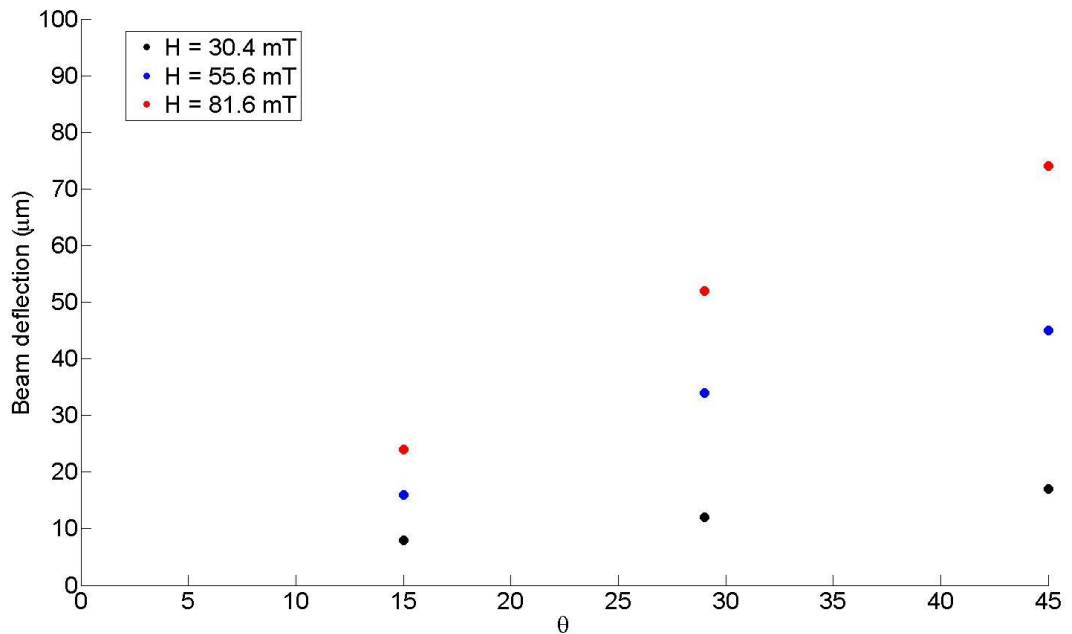

Figure 4.7 Experimental beam deflection of the microbeams at different orientations (θ) and field strength.

Chapter 5 Conclusions and Future Work

5.1 Conclusions

This work focused on the torque response of ferromagnetic prisms in uniform magnetic fields at macro and micro scales. The magnetic responses of different magnetic materials were outlined in chapter two and it was followed by the conceptual and mathematical description of induced magnetization in a ferromagnetic material in a spatially uniform magnetic field. The magnetization vector was then used to formulate the induced torque on a ferromagnetic prism in a magnetic field. It was analytically shown that the magnetic torque on a thin film Ni is a function of the orientation of the prism, magnitude of the applied magnetic field and the aspect ratio of the thin film. It was concluded that the induced torque is maximized for the angle of 45° between the magnetic field lines and the principal axis of the ferromagnetic prism. Also, the higher magnetic fields, $|\vec{H}|$, resulted in higher induced torque on the ferromagnetic prisms. In addition, it was shown that the induced torque is maximized for the aspect ratio of 0.317 which most effectively incorporates the effects of the magnetization magnitude and direction with the volume of the ferromagnetic prism. In chapter three, experimental macro scale beams were fabricated and tested in a uniform magnetic field to validate the analytical results. The beam bending deflection of the aluminum macro beams with square cuboid nickel masses affixed at the tip were measured in a uniform magnetic field as an indirect method to evaluate the induced magnetic torque on a nickel prism. The experimental results also illustrated that the beam deflection or equivalently, the induced torque is maximized at $\theta = 45°$ and it increases as the magnitude of the applied magnetic field increases. Furthermore, theory showed that torque is maximized when the aspect ratio of the prism is around 0.317, and a peak was seen in this range experimentally. In other words, the induced magnetic torque on a ferromagnetic square cuboid can be optimized if the

thickness of the thin-film prism designed to be about one third of the lateral length during the fabrication process. Experimental and theoretical data also showed that significant torque can still be generated at lower aspect ratios (0.15 – 0.317); therefore, extensive fabrication processes to incorporate high volumes of ferromagnetic materials in macro and micro scales can be avoided. As described in chapter four, micro scale beams with nickel prisms at the tip were fabricated and the beam deflection in a spatially uniform magnetic field was measured to explore the feasibility of using thin film ferromagnetic materials to generate torque in micro scale. Similar to the results in chapter three, the beam deflection for the microbeams maximized at $\theta = 45°$ and was dependent on the magnitude of the applied magnetic field. Therefore, by a precise control over the thickness of the deposited ferromagnetic prism, the thin film can be also actuated in micro scale which is useful in many MEMS applications.

5.2 Future work

The future work on this study may include thorough characterization of the sputtering and confinement of the ENP deposition process. Also, it is important to investigate the purity and uniformity of the volume of the Ni deposited during the electroless nickel plating. Furthermore, in order to determine the source of mismatch between the analytical predictions and experimental data in the microbeams, characterization experiments may be performed.

References

1. Abbott, J.J., et al., *Modeling magnetic torque and force for controlled manipulation of soft-magnetic bodies.* IEEE Transactions on Robotics, 2007. **23**(6): p. 1247-1252.
2. Sharma, P.V., *Demagnetization effect of a rectangular prism.* Geophysics, 1968. **33**(1): p. 132-134.
3. Kraus, L., *The demagnetization tensor of a cylinder.* Czechoslovak Journal of Physics, 1973. **23**(5): p. 512-519.
4. Beleggia, M., M. De Graef, and Y. Millev, *The equivalent ellipsoid of a magnetized body.* Journal of Physics D: Applied Physics, 2006. **39**(5): p. 891.
5. Beleggia, M., M. De Graef, and Y. Millev, *The Equivalent Ellipsoid of a magnetized body.* Journal of Physiscs D: Applied Physics, 2006: p. 891-899.
6. Beleggia, M. and M. De Graef, *On the computation of the demagnetization tensor field for an arbitrary particle shape using a Fourier space approach.* Journal of magnetism and magnetic materials, 2003. **263**(1): p. L1-L9.
7. Park, J. and M. Allen, *Development of magnetic materials and processing techniques applicable to integrated micromagnetic devices.* Journal of Micromechanics and Microengineering, 1998. **8**(4): p. 307.
8. Sadler, D.J., T. Liakapoulos, and C.H. Ahn, *A universal electromagnetic microactuator using magnetic interconnection concepts.* Journal of Microelectromechanical Systems, 2000. **9**(4): p. 460-468.
9. Vollmers, K., et al., *Wireless resonant magnetic microactuator for untethered mobile microrobots.* Applied Physics Letters, 2008. **92**(14): p. 144103.
10. Ivan, I.A., et al. *First experiments on magpier: A planar wireless magnetic and piezoelectric microrobot*. in *Robotics and Automation (ICRA), 2011 IEEE International Conference on*. 2011. IEEE.
11. Sitti, M., et al., *Biomedical applications of untethered mobile milli/microrobots.* Proceedings of the IEEE, 2015. **103**(2): p. 205-224.
12. Khalil, I.S., et al., *MagnetoSperm: A microrobot that navigates using weak magnetic fields.* Applied Physics Letters, 2014. **104**(22): p. 223701.
13. *SU-8 Permanent Photoresists* Available from: <u>http://www.microchem.com/pdf/SU-8-table-of-properties.pdf</u>.
14. *MEMScyclopedia*. 12/2013; Available from: <u>http://memscyclopedia.org/su8.html</u>.

Vita

Soroosh Torabi was born in Isfahan, Iran. He received his B.S. degree in Mechanical Engineering from Isfahan University of Technology, Isfahan, Iran in 2013. Then, he joined the Department of Mechanical Engineering at the University of Kentucky, Lexington, KY, for his graduate studies. He is currently a research assistant at the Precision BioSystems lab pursuing his master's and doctoral degree in mechanical engineering in the fields of micro robotics, microfluidics and microfabrication.